Eng. Sci., 2025, **38**, 1861

Engineered Science
DOI: https://dx.doi.org/10.30919/es1861

Non-Invasive Breast Cancer Detection Using Physics Informed Neural Networks with Thermal Imaging and 3D Patient-Specific Breast Models

Olzhas Mukhmetov,[1,7] Yong Zhao,[1] Aigerim Mashekova,[1] Dongming Wei,[2] Vasilios Zarikas,[3,4] Eddie YK Ng,[5,*] Amgad Salama,[1] Madina Shapatova[6] and Nurduman Aidossov[1]

Abstract

This study presents a novel non-invasive approach for breast cancer detection and tumor localization by developing an optimized Physics-Informed Neural Network (PINN) model integrated with infrared (IR) thermal imaging and 3D physical breast modeling. The proposed method leverages thermal data from an IR camera and anatomical information from a 3D scanner to train a PINN, incorporating the bioheat equation to perform both forward and inverse predictions. The PINN is uniquely optimized to estimate bio-physical parameters, such as tumor radius and depth, enabling accurate tumor diagnosis. Validation against Finite Element Met hod (FEM) simulations from ANSYS demonstrates that the PINN model achieves high accuracy, with error margins as low as 0.70% for radius and 1.38% for depth after training optimizations. Compared to traditional FEM solvers, the PINN model offers 10 times faster simulation post training, highlighting its computational efficiency. This work underscores the potential of PINNs as a promising tool for non-invasive breast cancer diagnostics, combining physical constraints, anatomical accuracy, and machine learning for enhanced tumor detection and localization.

Keywords: Breast cancer detection; Infrared thermal imaging; 3D breast modeling; Physics- informed neural networks (PINNs); Finite element method (FEM).
Received: 19 June 2025; Revised: 21 October 2025; Accepted: 03 November 2025
Article type: Research article.

1. Introduction

Breast cancer is the most common malignancy among women worldwide, with approximately 2.3 million new cases diagnosed annually.[1] A comprehensive study published in Nature Medicine in February 2025 provides updated global breast cancer statistics. According to this study, in 2022, there were approximately 2.3 million new cases of female breast cancer and 670,000 deaths worldwide. The study also projects a significant increase in breast cancer cases and deaths by 2050, with new cases expected to rise by 38% and deaths by 68%, disproportionately affecting low-Human Development Index (HDI) countries.[2] Early detection is crucial for improving survival rates, as breast tumors detected at an early stage can be treated with less aggressive therapies and have significantly better outcomes. According to the American Cancer Society (2023), the five-year survival rate for localized breast cancer is over 90%, whereas late- stage detection drastically reduces survival chances.[3]

Despite the advances in treatment, delayed diagnosis remains a global issue, particularly in low- resource settings where access to advanced screening technologies is limited.[4] The high cost and invasiveness of conventional imaging techniques pose additional challenges for large-scale implementation. Thus, there is a pressing need for non-invasive, cost-effective, and accurate diagnostic methods to facilitate early detection and improve clinical decision-making.[5]

Several tools are currently used for breast cancer diagnosis, each one associated with advantages and limitations. Mammography is the most widely used screening tool, offering high sensitivity for microcalcifications and

---

[1] *Department of Mechanical and Aerospace Engineering, School of Engineering and Digital Sciences, Nazarbayev University, Astana, 010000, Kazakhstan*
[2] *Department of Mathematics, School of Sciences and Humanities, Nazarbayev University, Astana, 010000, Kazakhstan*
[3] *Department of Mathematics, University of Thessaly, Volos, Thessaly, Greece*

abnormal masses. However, its effectiveness is reduced in women with dense breast tissue, leading to false negatives.[6] Moreover, mammography involves ionizing radiation exposure, limiting its use for frequent screenings.[7] Ultrasound is commonly used as a supplementary tool, especially in younger patients with dense breast tissues.[8] However, ultrasound's accuracy is highly operator-dependent, and its high false-positive rate can result in unnecessary biopsies.[9] Magnetic Resonance Imaging (MRI) offers superior soft tissue contrast and is highly sensitive for high-risk patients.[10] However, MRI is expensive, time- consuming, and has a non-negligible rate of false positives, leading to overdiagnosis and increased healthcare costs.[11] These limitations highlight the need for additional imaging modalities that, together with the previously mentioned standard techniques, will be able to reduce diagnostic errors, eliminate ionizing radiation exposure, and provide accurate tumor detection and localization at early stages.

Infrared thermal imaging, also known as thermography, is a noninvasive and radiation-free method for identifying temperature differences in breast tissue. Malignant tumors often display elevated metabolic activity and increased blood vessel formation, leading to localized heat emissions that infrared cameras can detect.[12] Unlike conventional imaging techniques, thermography reveals functional changes before the emergence of structural abnormalities, positioning it as a potentially effective early detection tool.[8] Integrating 3D breast modeling with IR thermal imaging provides a spatially accurate representation of the breast, allowing for better correlation between surface temperature patterns and internal tumor locations.[13] Physics- Informed Neural Networks (PINNs) further refine this approach by incorporating inverse heat transfer equations to estimate the depth and size of tumors based on surface temperature data.[14]

Furthermore, a multi-modal approach can significantly enhance the precision of non-invasive breast cancer diagnostics, reduce false positives and improving early-stage detection. While existing imaging modalities provide valuable diagnostic information, they often fail to localize tumors without invasive biopsies precisely. A sole thermal imaging lacks depth resolution, while mammography and MRI may yield false positives or negatives due to dense breast tissue.[15] Previous studies have extensively explored mammography, ultrasound, and MRI in breast cancer detection.[6,8] While these techniques have been effective, their limitations in sensitivity and specificity have driven interest in alternative imaging methods.

Several researchers have investigated thermal imaging as a non-invasive diagnostic tool. Arora *et al*. (2008) demonstrated the feasibility of using thermography for early detection, while Sinha *et al*. (2020) highlighted the challenges of standardization and interpretation.[12,13] Recent studies have focused on machine learning-based thermal analysis to enhance diagnostic accuracy.

3D modeling techniques have been widely applied in reconstructive surgery, prosthetics, and tumor localization.[14] In breast cancer diagnostics, 3D surfaces scanning combined with imaging modalities has been explored to improve tumor detection accuracy.[11]

Physics-informed neural Networks (PINNs) have gained attention for solving complex inverse problems in medical imaging.[15] Recent studies have shown that PINNs can model heat diffusion in biological tissues, making them highly applicable to tumor localization using thermal imaging and 3D models.

Pratama *et al*. (2023) propose a method called r-PINN-Adam, which integrates Physics-Informed Neural Networks (PINNs) with a restarting strategy to solve the partial differential equations (PDEs) governing thermal behavior in breast tissue. This approach is designed to model the temperature distribution in both normal and tumorous breast tissues, facilitating the identification of anomalies indicative of cancer. The application of r-PINN-Adam demonstrated improved accuracy in modeling the thermal behavior of breast tissue compared to the traditional methods. This advancement holds promise for enhancing non-invasive breast cancer screening techniques, potentially leading to earlier detection and better patient outcomes. However, the paper uses a simplified hemispherical model to represent the human breast, rather than a full anatomical or patient-specific breast geometry. Results on idealized models may not directly translate to real-world diagnostic accuracy without validation on medical imaging or patient- specific geometries.[16]

Mukhmetov *et al*. (2023) introduce a novel approach to modeling heat transfer in breast tissue using Physics-Informed Neural Networks (PINNs). This method aims to improve the speed and accuracy of temperature distribution predictions, which are crucial for non-invasive breast cancer diagnostics.

The key limitations of that work are that it focuses solely

---

[4] *Mathematical Sciences Research Laboratory (MSRL), Lamia, 35100, Greece*

[5] *School of Mechanical and Aerospace Engineering, Nanyang Technological University, 639798, Singapore*

[6] *Medical Center Hospital of the President's affairs Administration of the Republic of Kazakhstan, E495 build No 2, Astana, Kazakhstan*

[7] *School of Intelligent Systems, Astana IT University, Astana, 010000, Kazakhstan*

**Email:* mykng@ntu.edu.sg (Eddie YK Ng)

on forward simulations of temperature distribution in breast tissue. It does not address inverse problems, such as inferring tumor characteristics (*e.g.*, location, size, or thermal properties) from observed temperature data, which would be more clinically relevant for diagnostic purposes.[17]

A novel approach that combines thermal data with 3D breast modeling and PINN is proposed in the present study to improve localization accuracy. This paper also aims to demonstrate the potential efficiency of IR imaging, which provides real-time, non-invasive temperature data correlated with tumor metabolism. 3D breast modeling captures anatomical features, allowing for precise spatial mapping of thermal data. PINNs integrate physics-based constraints to infer internal heat sources, improving tumor localization accuracy.

2. Materials and methods

2.1 Materials and instruments

This study used infrared (IR) thermal imaging to capture breast surface temperature distributions. A Fluke TiS60+ thermal camera was selected due to its high resolution and sensitivity, which are crucial for detecting temperature variations associated with tumor-induced angiogenesis and metabolic activity. Imaging was conducted from multiple angles (frontal, lateral, and oblique) at a standardized focus distance of 1.5 meters, following established thermography protocols.[18,19,20]

Based on the Alder Lake architecture, all simulations and model training were performed on a desktop computer with an Intel Core i5-12400 processor featuring 6 cores and 12 threads. The system was fitted with an ASUS ROG STRIX NVIDIA GeForce RTX 4090 graphics card with 24 GB of GDDR6X memory, providing substantial computational power for deep learning and parallel processing tasks. Additionally, the machine was equipped with 32 GB of DDR4 RAM running at 3200 MHz, ensuring smooth execution of memory-intensive simulations and neural network training.

To create anatomically accurate 3D breast models, an XYZ Handheld 3D Scanner was used. This scanner employs structured light technology, capturing high-resolution surface geometry with an accuracy of up to 0.2 mm. The ability to generate a 360-degree surface mesh allows for precise mapping of thermal data onto a spatially accurate breast model, improving tumor localization and depth estimation.

The 3D scanning process involved the following steps:

1. Patient Positioning: Subjects were positioned in a neutral, upright stance to ensure an accurate anatomical representation.
2. Data Capture: The scanner was moved around the breast region, capturing multiple perspectives to generate a full 3D surface mesh. The optimal distance of scanning is 30 - 50 cm.
3. Post-Processing: The scanned data was processed using 3D reconstruction software to align and refine the mesh.

2.2 PINNs model

Physics-Informed Neural Networks (PINNs) are a class of neural networks that incorporate physical laws, in the form of partial differential equations (PDEs), into the learning process. Unlike conventional deep learning models, which rely purely on data, PINNs embed known physics knowledge directly in the loss function during training to improve model

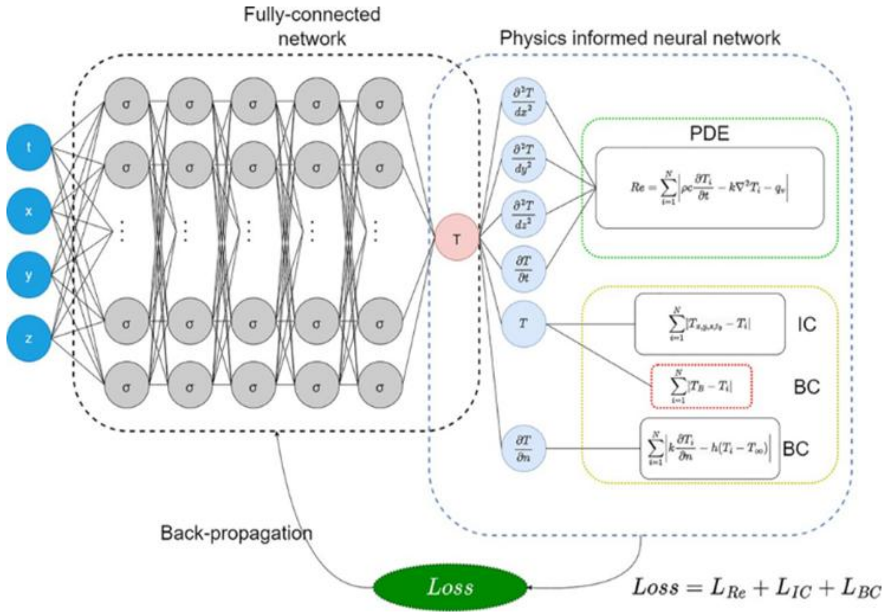

Fig. 1: The architecture of PINN.

improves generalization even with small datasets. PINNs operate without requiring meshing of the domain, unlike generalization and accuracy. This reduces overfitting and traditional Finite Element or Finite Difference methods. This makes them more scalable in high-dimensional PDEs and irregular domains. They rely on automatic differentiation to compute derivatives in PDE residuals. Thus, we can get seamless and precise gradient computation, unlike numerical differentiation.

In the context of breast cancer tumor localization, PINNs infer internal temperature distributions based on surface temperature obtained from infrared (IR) thermal imaging. The network takes as input the spatial coordinates (x, y, z) and time (t) and predicts the temperature distribution T (x, y, z, t) within the breast tissue.

As shown in Fig. 1, the PINN architecture consists of Eq. (1):

$$\mathcal{L}_{\text{total}} = \mathcal{L}_{\text{data}} + \lambda_{\text{PDE}} \cdot \mathcal{L}_{\text{PDE}} + \lambda_{\text{BC}} \cdot \mathcal{L}_{\text{BC}} + \lambda_{\text{IC}} \cdot \mathcal{L}_{\text{IC}} \qquad (1)$$

where:

$\mathcal{L}_{\text{data}}$: loss forming from fitting observed data

$\mathcal{L}_{\text{PDE}}$: residual loss enforcing the physics

$\mathcal{L}_{\text{BC}}$: boundary conditions loss

$\mathcal{L}_{\text{IC}}$ initial conditions loss (for time-dependent problems)

λ: tunable weights for each component

- A fully connected neural network that maps input coordinates (x, y, z, t) to temperature TT.
- Physics-informed layers that enforce heat transfer equations, boundary conditions (BCs), and initial conditions (ICs).
- A loss function that combines residual errors *(L_{Re})* from PDEs, ICs, and BCs to improve training efficiency.
- Back-propagation is used to adjust weights and minimize the overall loss, ensuring compliance with experimental data and physical laws.

2.3 Governing physics equations

The heat transfer in biological tissue follows the bioheat equation, a modified form of Fourier's heat conduction equation. The governing PDE, assuming negligible blood perfusion, used in PINN modeling is Eq. (2):

$$\rho c\,\frac{\partial T}{\partial t} - k\nabla^2 T = q_v \qquad (2)$$

where:

ρ is the tissue density $[kg/m^3]$.

c is the specific heat capacity $[J/kg\ K]$.

k is the thermal conductivity of the breast tissue $[W/m\ K]$.

T is the temperature distribution in the tissue $[K]$.

q_v represents internal heat generation, which is higher in tumor regions due to increased metabolic activity and angiogenesis $[W/m^3]$.

In the image, this PDE is enforced within the Physics-Informed Neural Network (PINN) to ensure that the learned temperature distribution adheres to the heat transfer laws in biological tissues.

Additionally, the model must satisfy initial and boundary conditions (ICs & BCs):

Initial Condition (IC): Defines the baseline temperature distribution at time t=0 Eq. (3).

$$\sum_{i=1}^{N} \left| T_{x,y,z,t=0} - T_i \right| \qquad (3)$$

Boundary Conditions (BCs): Ensures proper convective heat dissipation at the skin surface and interactions with surrounding tissues. Ignore heat radiation mode Eq. (4) and Eq. (5):

$$\sum_{i=1}^{N} \left| T_B - T_i \right| \qquad (4)$$

$$k\,\frac{\partial T_i}{\partial n} - h(T_i - T_\infty) = 0 \qquad (5)$$

(breast convective heat surface only)

where h is the skin boundary's convective heat transfer coefficient $[W/m^2K]$, bound to the ambient temperature, TB is temperature at the breast chest wall. This term indicates a comparison (or loss) between predicted temperature and a known reference temperature (breast chest wall temperature). This is a Dirichlet condition because the temperature is prescribed at this location. The convective heat flux from the skin to the environment is a Neumann BC since it involves the derivative of temperature normal to the surface.

The total loss function in the PINN model combines the residuals from the PDE, ICs, and BCs Eq. (6):

$$Loss = L_{Re} + L_{IC} + L_{BC} \qquad (6)$$

This loss function ensures that the PINN solution matches both experimental data and the known physics of heat transfer.

2.4 Implementation process

The proposed method of integration of IR thermal imaging and 3D breast modeling within the PINN framework follows these steps (Fig. 2):

1. Thermal Data Acquisition:

The Fluke TiS60+ thermal camera captures surface temperature distributions of the breast.

These images are processed to extract key thermal features, including regions of increased heat emission that may indicate tumor presence.

2. 3D Model Generation:

The XYZ Handheld 3D Scanner reconstructs an anatomically accurate 3D breast model.

The 3D model provides spatial constraints for mapping temperature data onto the breast surface.

3. Transferring an infrared (IR) image onto a 3D geometry of a breast model involves a texture mapping or data projection process that aligns the 2D IR data (temperature image) with the 3D surface geometry. The IR image is calibrated (pixel values correspond to temperature) and is in a PNG format. Mapping the 2D pixel coordinates (u, v) to the 3D surface coordinates (x, y, z) using intrinsic/extrinsic camera parameters or assumed orthographic projection. Perform manual registration: Use anatomical landmarks (*e.g.*, nipple, tumor hotspot) to co-register.

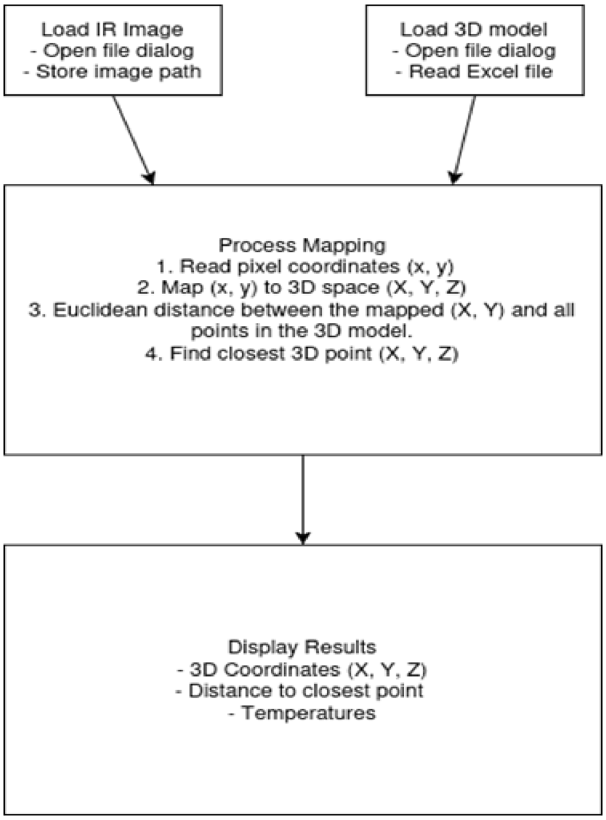

Fig. 2: Flow chart of integration IR, 3D scans and PINN.

A Python-based tool was developed to map infrared (IR) image temperatures to a 3D model of a breast, integrating spatial coordinate mapping. The 3D model, provided as X, Y, Z coordinates (in meters) in an Excel file, was loaded using pandas. The IR image, a 2D thermal map in PNG format, was processed with PIL (Pillow) to extract pixel data. The mapping process involved normalizing the pixel coordinates to the 3D model's X-Y range, assuming a frontal view (X-Y plane). The closest 3D point was identified by calculating the Euclidean distance in the XY plane using numpy. The Euclidean distance is computed in the XY plane to find the nearest point in the 3D model to the mapped coordinates from the IR image. Z-coordinate is ignored since the IR image is 2D and looking for the closest point on the surface in the XY plane. (*Supporting information file*) Eq. (7).

$$\sqrt{(X - x_{3D})^2 + (Y - y_{3D})^2} \tag{7}$$

4. PINN Training with Spatial and Thermal Constraints:

The 3D model provides geometrical input constraints to the PINN, ensuring the network learns from realistic anatomical structures.

The thermal data provides boundary conditions for the heat equation, guiding the model toward accurate internal temperature estimations.

The PINN predicts internal temperature distributions, allowing for precise tumor depth and size estimation.

PINN enhances tumor localization accuracy by incorporating physical laws, anatomical constraints, and real-world thermal data, reducing false positives and improving diagnostic reliability.

This study employs Physics-Informed Neural Networks (PINNs) to solve the transient heat conduction problem in a complex 3D geometry with a localized heat source. The proposed framework integrates physical laws, experimental temperature measurements, and trainable source parameters (depth and radius) into a unified neural network model using the DeepXDE library and PyTorch backend.

2.4.1 Geometry acquisition and preprocessing

The computational domain is constructed using a custom 3D point cloud extracted from a surface geometry txt file. The spatial coordinates (X, Y, Z) are non-dimensionalized using a characteristic length scale. Boundary points are identified by detecting nodes near the z=0 plane. These boundary points are used to impose Dirichlet boundary conditions.

2.4.2 Thermophysical parameters and non-dimensionalization

The thermal properties of the medium are defined by the product density and specific heat capacity(ρc) and the thermal conductivity (k). From these, the thermal diffusivity $\alpha = k/\rho c$ is computed. A reference temperature and a characteristic time scale $\tau = L^2/\alpha$ are used to render all quantities dimensionless (analogised to Lumped system analysis with small Biot number), allowing for stable training and easier parameter tuning.

2.5 Heat source modeling

The internal heat generation in this study is modeled as a localized spherical heat source embedded within the domain. The non-dimensional heat source $Q(x,y,z)$ is defined as Eq. (8):

$$Q(x,y,z) = \frac{q_0}{\frac{4}{3}\pi R^3}, if\ r = \sqrt{(x-x_0)^2 + (y-y_0)^2 + (z-z_0)^2} \leq r^* \quad (8)$$

where:

q_0 is the non-dimensionalized power input.

r* is the non-dimensional radius of the heat source Q (x, y, z).

(x_0,y_0,z_0) is the center of the source, where $z_0=depth$ is a trainable parameter.

r is the Euclidean distance from a point (x,y,z) to the source center. R is the euclidean radius of the heating zone

To ensure differentiability and compatibility with gradient-based training, this expression is approximated using a smooth Heaviside-like formulation Eq. (9):

$$Q(x,y,z) = \frac{q_0}{\frac{4}{3}\pi R^3} . ReLU\left(1 - \frac{r}{r^*}\right) \quad (9)$$

Where Eq. (10):

$$ReLU(x) = max(0,x) \quad (10)$$

This expression ensures that the source has a smooth boundary (zero outside the radius) and maintains continuity of gradients, which is essential for training neural networks via backpropagation.

A fully connected neural network (FNN) with 5 hidden layers of 256 neurons each and a *tanh* activation function is used to approximate the solution. The input vector includes spatial and temporal coordinates (x, y, z, t) and the output is the predicted non-dimensional temperature.

Training is conducted in two stages:

1. Stage 1: Adam Optimizer

The model is initially trained using the Adam optimizer for 5000 iterations with separate learning rates for the network weights ($lr = 0.0001$) and the source parameters ($lr = 0.0002$).

2. Stage 2: Limited Broyden–Fletcher–Goldfarb–Shanno algorithm (L-BFGS) Fine-Tuning To refine the solution and improve convergence, L-BFGS optimization is applied iteratively (up to 5 times or until convergence), optimizing both the network and the trainable source parameters.

3. Results

Two temperature distribution models were developed: one using ANSYS[20] and the other using a PINN-based approach. Both models utilized identical initial and boundary conditions to ensure comparability. The ANSYS model employed a meshed finite element solver with predefined material properties and bioheat conduction equations. The PINN model was trained to solve the bioheat equation by minimizing a physics-informed loss function that incorporates PDE residuals, initial & boundary conditions, and data points obtained from the ANSYS simulation.[20]

Fig. 3a illustrates the temperature distribution obtained from the ANSYS simulation, while Fig. 3b presents the corresponding results from the PINN model.

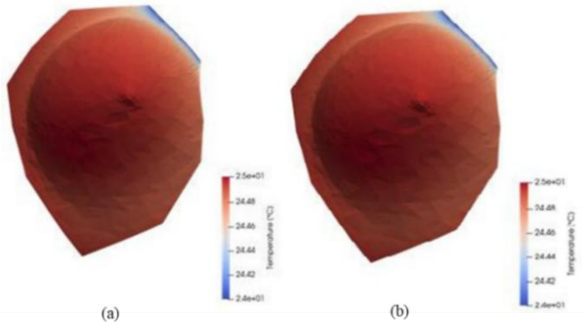

Fig. 3: (a) ANSYS simulation results of breast #1,(b) PINN simulation results breast #1.

Both models exhibit similar spatial temperature distributions on the skin surface of the breast, with the highest temperature regions localized at the center and gradually declining towards the periphery. The PINN model captures the overall heat distribution, demonstrating its ability to approximate the underlying physics. The color scale in both models ranges from approximately

24.4°C to 25°C, indicating that the PINN model effectively learns the thermal behavior. However, slight discrepancies in temperature intensities suggest that localized refinements in PINN training, such as adaptive learning rates or enhanced neural network architectures, could enhance precision.

Table 1: Comparison of actual and computed parameters (radius, depth, conductivity of the tumor), real breast geometry #1.

PINN results	real	computed	error %
radius [m]	0.00428	0.004429	3.48
depth [m]	0.027	0.027627	2.32
k [$W/m\ K$]	0.625	0.69444	11.11

The radius shows a 3.48% deviation, indicating that the PINN model slightly overestimates the region's size. The depth has a minor 2.32% deviation, suggesting that the PINN model provides a relatively accurate prediction for depth. Both error values are within an acceptable range for approximation models with 5%, though further refinement of training data and loss function optimization could help reduce these deviations (Table 1).

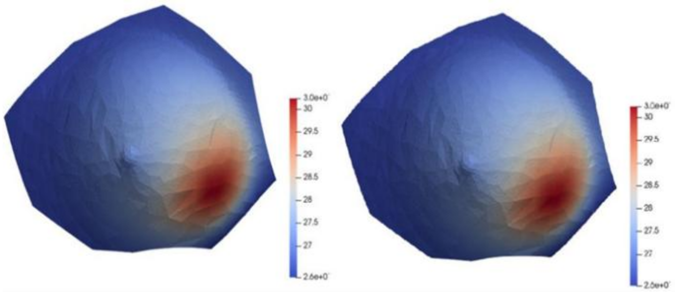

(a) (b)

Fig. 4: (a) ANSYS simulation results of breast #2, (b) PINN simulation results breast #2.

Fig. 4 presents the temperature distributions case #2 obtained from the ANSYS and PINN models. Both models demonstrate a consistent spatial distribution, with the highest temperature regions (red) concentrated in a localized area. The PINN model successfully approximates the overall thermal behavior of the ANSYS simulation.

Table 2: Comparison of actual and computed parameters (radius, depth, conductivity of the tumor), real breast geometry #2.

PINN results	real	computed	error %
radius [m]	0.00524	0.00500	4.58
depth [m]	0.027	0.0284	5.19
k [$W/m\ K$]	0.625	0.6783	8.53

The radius exhibits a 4.58% error, with the PINN model slightly underestimating the actual value. The depth has a 5.19% error, with the PINN model slightly overestimating the proper depth. The results indicate that the PINN model successfully captures the overall shape and thermal distribution, but up to 5.19% deviations suggest that further refinement of depth is needed (Table 2).

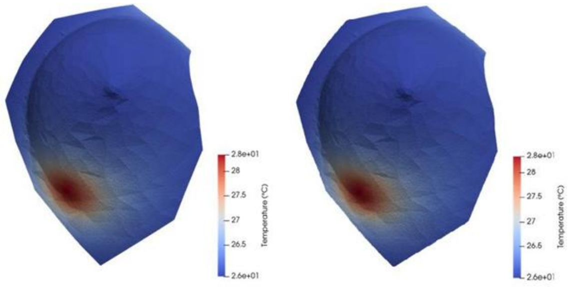

(a) (b)

Fig. 5: (a) ANSYS simulation results of breast #3, (b) PINN simulation results breast #3.

Both models exhibit a similar spatial temperature distribution of case #3, with a localized region of elevated temperature (red) surrounded by lower-temperature areas (blue) (see Fig. 5). The PINN model successfully captures the general temperature distribution observed in the ANSYS model. Some deviations are observed near the domain boundaries in the PINN model, which may be attributed to limitations in enforcing boundary conditions within the neural network framework.

Table 3: Comparison of actual and computed parameters (radius, depth, conductivity of the tumor), real breast geometry #3.

PINN results	real	computed	error %
radius [m]	0.00458	0.00454	0.70
depth [m]	0.032	0.031	1.38
k [W/mK]	0.625	0.68425	9.48

The radius has a very low error of 0.70% of case #3, indicating that the PINN model provides a highly accurate approximation. The depth shows a slightly higher 1.38% error, which still falls within an acceptable range for numerical modeling. Compared to the previous results, this dataset demonstrates a significant improvement in accuracy, suggesting better PINN training convergence. The low deviation in radius (0.70%) and depth (1.38%) indicates that PINNs can effectively replicate FEM-based results with minimal discrepancy (Table 3).

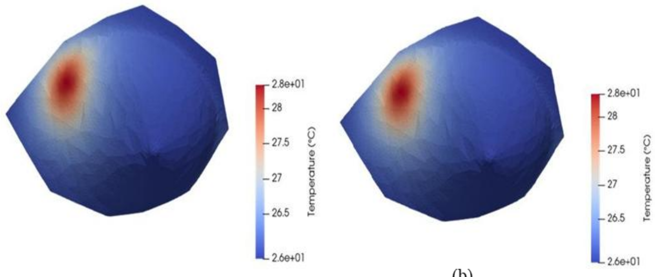

(a) (b)

Fig. 6: (a) ANSYS simulation results of breast #4, (b) PINN simulation results breast #4.

Fig. 6 illustrates the temperature distribution results for a thermally simulated domain of case #4, with Figure 6a corresponding to the ANSYS model and Figure 6b to the PINN model. Both models display a localized region of elevated temperature, visualized in red, surrounded by cooler regions shown in blue. The temperature anomaly is concentrated in the upper left region of the model, with consistent spatial orientation and shape across both simulations (Table 4).

Table 4: Comparison of actual and computed parameters (radius, depth, conductivity of the tumor), real breast geometry #4.

PINN results	real	computed	error %
radius [m]	0.00623	0.00614	1.44
depth [m]	0.032	0.0315	1.38
k [$W/m\ K$]	0.625	0.65342	4.55

To evaluate the practical applicability of the Physics-Informed Neural Network (PINN) model compared to the Finite Element Method (FEM)-based ANSYS solver, a comparison of computational time was conducted. The results are summarized in the table below:

Table 5: ANSYS vs PINN: GPU time spent on simulations.

	training [s]	simulation [s]	total time [s]
ANSYS (case 1)	0	260	260
PINN (case 1)	300	20	320
ANSYS (case 2)	0	240	240
PINN (case 2)	265	15	280
ANSYS (case 3)	0	275	275
PINN (case 3)	290	15	305
ANSYS (case 4)	0	320	320
PINN (case 4)	320	25	345

The ANSYS model does not require a training phase but incurs a relatively high simulation cost of 260 seconds, due to the complexity of mesh generation and numerical PDE solving. The PINN model, in contrast, requires an initial training time of 300 seconds, but achieves a rapid simulation time of only 20 seconds once trained (Table 5). While the total time for PINN is slightly higher than ANSYS in this instance, the advantage of PINNs becomes significant in scenarios involving multiple simulations, where repeated inferences can be performed without retraining.

Fig. 7 presents the evolution of training and testing losses over the course of 5000 optimization steps. Both loss curves exhibit a consistent and smooth decrease, indicating stable convergence of the model. The initial loss drops rapidly by several orders of magnitude within the first few hundred steps, followed by a slower but steady decline, eventually reaching values below 10−6.

4. Real case study

The model was tested on a real case (see Fig. 8). Patient is a 54-year-old Kazakh woman, with diagnosed right breast cancer, in the upper right quarter. The mammary glands are asymmetric. The skin and nipples are unchanged. There is no nipple discharge. Visually, the entire right breast is occupied by a tumor with a diameter of 15 cm of dense consistency and crimson color. Peripheral lymph nodes are not palpable. The depth is not stated in the doctor's conclusion. The room temperature during the taking of the IR image was 26 degrees Celsius.

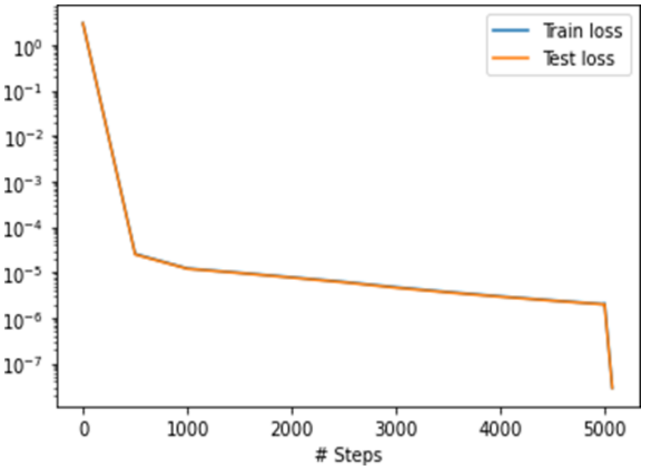

Fig. 7: Convergence of PINN (Loss vs Epochs).

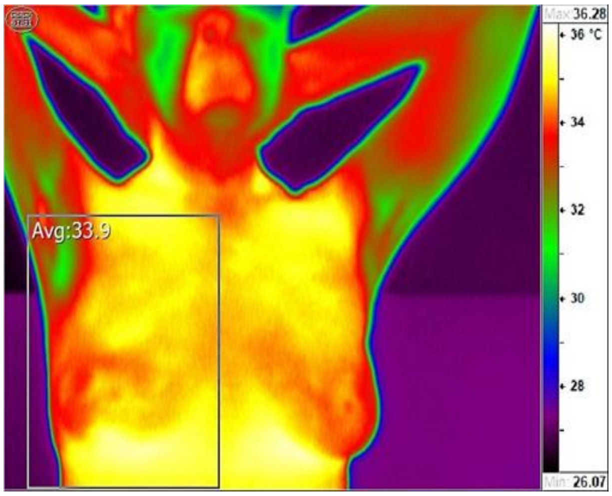

Fig. 8: IR image of the patient.

The IR image and 3D geometry of the real patient were used in PINN simulation to compute and compare the radius and depth of the tumor. The temperature on the skin surface was set as a Dirichlet boundary condition, so that the optimizer will tend to reach the same temperature profile on the skin surface as in a real patient case (see Fig. 9 and 10).

Fig. 11 demonstrates temperature distribution on the breast skin surface. Fig. 11b is the real breast IR image, while Fig. 11a and 11c are computed results of ANSYS and PINN. In the real case, there are some disturbances because of the veins inside the body. Computed temperature profiles are ideal because they do not include the presence of veins. However, the general temperature distribution and location of the hotspot (tumor) are the same in all three cases.

Fig. 9: 3D scanned model of the breast.

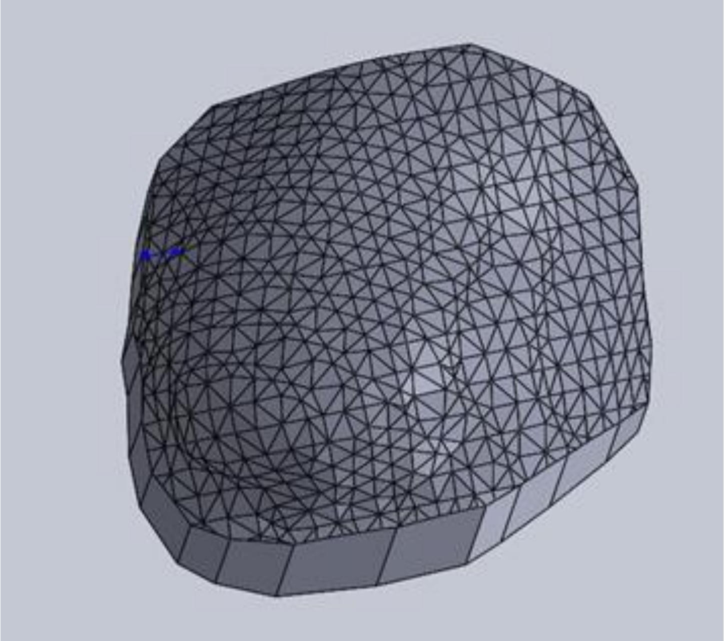

Fig. 10: Full-fledged 3D model of the breast.

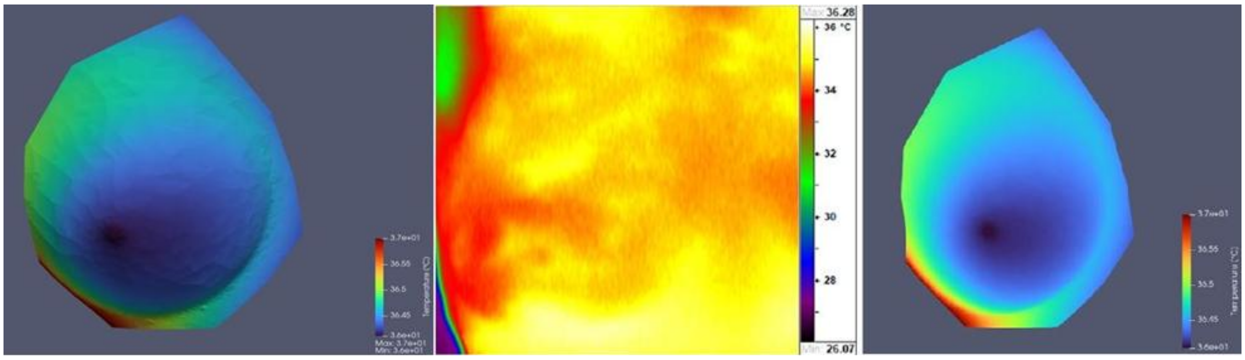

(a) (b) (c)

Fig. 11: (a)(b)(c) Temperature distribution from Ansys simulation, IR image of the patient's breast, Temperature distribution from PINN simulation.

Table 6: Comparison of real and computed parameters.

PINN results	real	computed	error %
radius	0.0075	0.008900	18.67
depth	unknown	0.036500	

Table 6 is the comparison between real and computed geometrical parameters of the analyzed feature. The computed radius shows an 18.67% deviation from the real value. The depth could not be experimentally determined and is therefore listed as unknown.

Table 7: ANSYS vs PINN: GPU time spent on simulations.

	training [s]	simulation [s]	total time [s]
ANSYS (case 1)	0	360	360
PINN (case 1)	410	20	420

Table 7 is the comparison of computational time between traditional finite element analysis using ANSYS and a Physics-Informed Neural Network (PINN). While ANSYS performs the simulation directly without a training phase, the PINN method requires initial training but significantly reduces simulation time.

5. Conclusion

This study presents the development of a novel Physics-Informed Neural Network (PINN) model designed to perform both forward and inverse predictions of temperature distributions, with applications in tumor diagnosis. Unlike traditional approaches, the proposed PINN framework leverages physical laws and boundary data to approximate thermal behavior and identify key parameters such as the radius and depth of temperature anomalies. While Finite Element Method (FEM) simulations are used in this work, they are not served as a comparative benchmark, but as a validation tool for assessing the accuracy and robustness of the PINN results.

The quantitative comparison demonstrates that the PINN model successfully captures the primary features of the ANSYS results, with error margins ranging from 0.70% to 5.19%, depending on the dataset. Initial results indicated deviations up to 5.19% in depth and 4.58% in radius, highlighting challenges in neural network generalization and boundary conditions enforcement. However, subsequent refinements in training strategies, loss function optimization, and data resolution led to significant improvements, reducing errors to as low as 0.70% for radius and 1.38% for depth, achieving near parity with the FEM results.

A real patient case was used to evaluate the practical performance and diagnostic potential of the proposed Physics-Informed Neural Network (PINN) model integrated with thermal imaging and 3D anatomical modeling. The patient was a 54-year-old Kazakh woman diagnosed with breast cancer located in the upper right quadrant of the right breast. The visible tumor exhibited a diameter of approximately 15 cm, with distinct coloration and firm consistency. This complex clinical presentation offered an ideal scenario to test the model's capability to handle realistic, patient-specific data. After training and optimization, the PINN predicted tumor radius 0.0089 meters, while clinically observed radius is 0.0075 meters, so the computed error is 18.67%. Tumor depth is 0.0365 meters (depth was not clinically recorded, so no direct error comparison is available). Although the model slightly overestimated the tumor radius, the hotspot location and temperature patterns closely matched the observed IR image and FEM-based ANSYS simulations. Notably, the deviation in radius (18.67%) is higher than the error range in simulated geometries (0.70–5.19%), likely due to the presence of unmodeled biological complexity such as blood vessels, heterogeneous tissue properties, and scanning artifacts. Despite the longer total time due to initial training, PINN offers significant scalability benefits, allowing repeated simulations and real-time analysis without re-training.

The results demonstrate that the PINN model can accurately capture the thermal patterns and anomaly characteristics validated by FEM simulations, achieving low error margins following training optimizations. This capability underscores the potential of PINNs as efficient and scalable tools for biomedical diagnostics, particularly in non-invasive tumor detection via thermal imaging. Moving forward, the integration of PINNs into biomedical workflows may offer a promising direction for real-time, patient-specific data-driven thermal analysis that is both computationally efficient and grounded in physical principles.

As a final note, thermography is useful as an adjunct method to traditional imaging since the latter was not inconclusive but adding the physiological dimensions shown by thermography allowed for another monitoring parameter to be introduced into the protocol. The role of breast thermography (if extended) in monitoring therapeutic response, especially in the context of oncological management, is suggested as future work. Indeed, the notion of tracking both anatomical tumor regression and correlated thermal patterns reflects a multidimensional approach to clinical surveillance that is highly valuable, particularly when aiming for individualized, response-guided protocols. Yes, this work was published, and we are in early stages of validation with FEM predictions, but we should encourage its scientific development and integration further. Many clinicians in conventional settings still perceive breast thermography as valid only when other methods fall short, and we believe it is pedagogically valuable to highlight here and then deconstruct that assumption.

Acknowledgments

This research was supported by Ministry of Science and Higher Education of the Republic of Kazakhstan grant #AP19678197 and Nazarbayev University under Faculty-development competitive research grants program for 2023 -

2025 Grant #20122022FD4126.

Conflict of Interest

The authors declare that the research was conducted in the absence of any commercial or financial relationships that could be construed as a potential conflict of interest.

Supporting Information

Applicable.

CRediT Statement

Olzhas Mukhmetov and **Michael Yong Zhao:** Conceptualization. **Olzhas Mukhmetov:** Investigation. **Dongming Wei** and **Michael Yong Zhao:** Methodology and Formal analysis. **Michael Yong Zhao** and **Dongming Wei:** Funding acquisition. **Olzhas Mukhmetov** and **Nurduman Aidossov:** Software development. **Olzhas Mukhmetov:** Validation. **Madina Shapatova:** Data collection. **Olzhas Mukhmetov**: Writing - Original draft. **Michael Yong Zhao, Dongming Wei** and **Eddie YK Ng**, **Vasilios Zarikas**, **Aigerim Mashekova** and **Amgad Salama:** Review, Editing and Final approval.

References

[1] H. Sung, J. Ferlay, R. L. Siegel, M. Laversanne, I. Soerjomataram, A. Jemal, F. Bray, Global cancer statistics 2020: GLOBOCAN estimates of incidence and mortality worldwide for 36 cancers in 185 countries, *CA: A Cancer Journal for Clinicians*, 2021, **71**, 209-249, doi: 10.3322/caac.21660.

[2] J. Kim, A. Harper, V. McCormack, H. Sung, N. Houssami, E. Morgan, M. Mutebi, G. Garvey, I. Soerjomataram, M. M. Fidler-Benaoudia, Global patterns and trends in breast cancer incidence and mortality across 185 countries, *Nature Medicine*, 2025, **31**, 1154-1162, doi: 10.1038/s41591-025-03502-3.

[3] American Cancer Society, Breast cancer facts & figures, Retrieved from www.cancer.org, 2023.

[4] F. Bray, J. Ferlay, I. Soerjomataram, R. L. Siegel, L. A. Torre, A. Jemal, Global cancer statistics 2018: GLOBOCAN estimates of incidence and mortality worldwide for 36 cancers in 185 countries, *CA: A Cancer Journal for Clinicians*, 2018, **68**, 394-424, doi: 10.3322/caac.21492.

[5] E. Y.-K. Ng, A review of thermography as promising non-invasive detection modality for breast tumor, *International Journal of Thermal Sciences*, 2009, **48**, 849-859, doi: 10.1016/j.ijthermalsci.2008.06.015.

[6] R. F. Brem, M. J. Lenihan, J. Lieberman, J. Torrente, Screening breast ultrasound: past, present, and future, *American Journal of Roentgenology*, 2015, **204**, 234-240, doi: 10.2214/ajr.13.12072.

[7] H. D. Nelson, M. Pappas, A. Cantor, J. Griffin, M. Daeges, L. Humphrey, Harms of breast cancer screening: systematic review to update the 2009 U.S. preventive services task force recommendation, *Annals of Internal Medicine*, 2016, **164**, 256-267, doi: 10.7326/m15-0970.

[8] W. A. Berg, Combined screening with ultrasound and mammography vs mammography alone in women at elevated risk of breast cancer, *Jama*, 2008, **299**, 2151, doi: 10.1001/jama.299.18.2151.

[9] S. Wojcinski, A. Farrokh, S. Weber, A. Thomas, T. Fischer & P. Hillemanns, The diagnostics of breast cancer with multiparametric ultrasound, *Archives of Gynecology and Obstetrics*, 2013, **288**(1), 21-26, doi: 10.1007/s00404-012-2532-5.

[10] C. Kuhl, The Current status of breast MR imaging part I. choice of technique, image interpretation, diagnostic accuracy, and transfer to clinical practice, *Radiology*, 2007, **244**, 356-378, doi: 10.1148/radiol.2442051620.

[11] N. H. G. M. Peters, I. H. M. Borel Rinkes, N. P. A. Zuithoff, W. P. T. M. Mali, K. G. M. Moons, P. H. M. Peeters, Meta-analysis of MR imaging in the diagnosis of breast lesions, *Radiology*, 2008, **246**, 116-124, doi: 10.1148/radiol.2461061298.

[12] N. Arora, D. Martins, D. Ruggerio, E. Tousimis, A. J. Swistel, M. P. Osborne, R. M. Simmons, Effectiveness of a noninvasive digital infrared thermal imaging system in the detection of breast cancer, *The American Journal of Surgery*, 2008, **196**, 523-526, doi: 10.1016/j.amjsurg.2008.06.015.

[13] N. Sinha, R. Nanda, & S. Gupta, Role of thermal imaging in early detection of breast cancer, *Infrared Physics & Technology*, 2020, **105**, 103243, doi: 10.1016/j.infrared.2020.103243.

[14] A. Sadeghi-Naini, O. Falou, H. Tadayyon, A. Al-Mahrouki, W. Tran, & M. C. Kolios, Quantitative ultrasound assessment of tumor cell death response in locally advanced breast cancer patients receiving chemotherapy, *Clinical Cancer Research*, 2013, **19**(8), 2163-2174, doi: 10.1158/1078-0432.CCR-12-2726.

[15] M. Raissi, P. Perdikaris, G. E. Karniadakis, Physics-informed neural networks: a deep learning framework for solving forward and inverse problems involving nonlinear partial differential equations, *Journal of Computational Physics*, 2019, **378**, 686-707, doi: 10.1016/j.jcp.2018.10.045.

[16] D. A. Pratama, M. A. Bakar, N. F. Ibrahim, R. Idris, N. Mohamed, Physical restriction neural networks with restarting strategy for solving mathematical model of thermal heat equation for early diagnose breast cancer, *Results in Applied Mathematics*, 2023, **19**, 100384, doi: 10.1016/j.rinam.2023.100384.

[17] O. Mukhmetov, Y. Zhao, A. Mashekova, V. Zarikas, E. Y. K. Ng, N. Aidossov, Physics-informed neural network for fast prediction of temperature distributions in cancerous breasts as a potential efficient portable AI-based diagnostic tool, *Computer*

Methods and Programs in Biomedicine, 2023, **242**, 107834, doi: 10.1016/j.cmpb.2023.107834.

[18] Ng EY, Chen Y, Ung LN, Computerized breast thermography: study of image segmentation and temperature cyclic variations, *Journal of Medical Engineering & Technology*, 2001, **25**(1),12-6. doi: 10.1080/03091900010022247.

[19] A. Mashekova, Y. Zhao, E. Y. K. Ng, V. Zarikas, S. C. Fok, O. Mukhmetov, Early detection of the breast cancer using infrared technology–A comprehensive review, *Thermal Science and Engineering Progress*, 2022, **27**, 101142, doi: 10.1016/j.tsep.2021.101142.

[20] O. Mukhmetov, D. Igali, A. Mashekova, Y. Zhao, E. Y. K. Ng, S. C. Fok, S. L. Teh, Thermal modeling for breast tumor detection using thermography, *International Journal of Thermal Sciences*, 2021, **161**, 106712, doi: 10.1016/j.ijthermalsci.2020.106712.

Open Access